J Seismol (2024) 28:555–577
https://doi.org/10.1007/s10950-024-10205-8

RESEARCH

Hypocenter uncertainty analysis of induced and tectonic earthquakes in the Netherlands

Jesper Spetzler · Elmer Ruigrok · Dagmar Bouwman

Received: 1 November 2023 / Accepted: 1 March 2024 / Published online: 10 April 2024

Abstract Induced earthquakes tend to be shallow, while tectonic events often occur in deeper parts of the Earth. A well-estimated hypocenter with uncertainties may help to evaluate whether an event is of an induced or tectonic origin. In this study, we focus on the development of a hypocenter method that helps to better define the source location of an earthquake and reduce the spatial error of the measurement. The hypocenter and the uncertainty is obtained by using the P- and S-wave phase time difference for a station and the P-wave traveltime differences between pairs of stations simultaneously in the hypocenter analysis. The uncertainty inherent to an imperfect reference velocity model, modelling, instrumental inaccuracy and phase time picking is propagated into the spacial hypocenter solution. A refined hypocenter methodology is successfully tested in a synthetic experiment with shallow (∼ 5 km), intermediate (∼ 10 km) and deep source points (∼ 15 km). The synthetic experiment indeed shows that it is possible to separate earthquakes by their depth solution, hence offering an indication that the event is either induced or tectonic. Case studies are presented of estimations of hypocenters and error ellipses for (1) induced seismicity at sites for gas storage in salt domes, geothermal production and gas extraction as well as (2) tectonic events.

Keywords Seismology · Earthquake location · Hypocenter uncertainty · Induced and Tectonic earthquakes

Elmer Ruigrok and Dagmar Bouwman contributed equally to this work.

Highlights
- A combination of differences between P- and S-time picks per station and P-time picks per two stations allows for a focused hypocenter solution.
- The uncertainty associated to the hypocenter is estimated from the 95 % confidence area of the 3D objective function.
- The hypocenter solution for induced earthquakes due to gas storage, gas extraction and geothermal activities as well as for tectonic events are estimated.

Supplementary Information The online version contains supplementary material available at https://doi.org/10.1007/s10950-024-10205-8.

J. Spetzler (✉)
Research Department of Seismology and Acoustics, Royal Netherlands Meteorological Institute, Utrechtseweg 297, 3731 GA De Bilt, The Netherlands
e-mail: jesper.spetzler@knmi.nl

E. Ruigrok
Department of Earth Sciences, Utrecht University, Princetonlaan 8a, 3594 CB Utrecht, The Netherlands
e-mail: elmer.ruigrok@knmi.nl

D. Bouwman
Department of Acoustics, Dutch National Institute for Public Health and the Environment, Antonie van Leeuwenhoeklaan 9, 3721 MA Bilthoven, The Netherlands
e-mail: dagmar.bouwman@rivm.nl

1 Introduction

Most published earthquake catalogues provide information about the magnitude, origin time, epicenter and depth. Uncertainties of earthquake properties are sometimes given. The error in the epicenter estimation may be small since it is usually not difficult to determine the lateral coordinates of an earthquake provided a proper azimuthal and distance distribution of stations. On the other hand, it can be difficult to estimate the source depth of the event. Several sources of uncertainty play a role for determination of hypocenter depth such as inaccuracies in the reference velocity model, the type of modelling, instrumentation and phase time picking (Ruigrok et al. 2023). All these different errors contribute to a misfit in timing between the modelled and observed traveltime picks. Local and regional seismicity is detected by receivers at or near the Earth's surface as oppositely to seismic well experiments and global seismology with stations distributed in depth, too (or on the other side of the Earth). In local and regional hypocenter experiments, errors in timing are mostly propagated into uncertainties in depth.

Natural earthquakes are found worldwide especially near tectonic plate boundaries and have existed for a long time throughout Earth's geological history. Induced seismicity is observed at many places where due to the production of natural resources, the subsurface stress conditions being alternated. An earthquake is more likely to take place when the subsurface stress field reaches the critical point of failure. In North America (magnitudes, $M > 3$), induced earthquakes due to wastewater disposal are often detected in Oklahoma, Texas, British Colombia and Alberta (Schoenball et al. 2017; Savvaidis et al. 2017; Eaton and Eyre 2017). On the European continent, sites for gas extraction near Pau, France and Groningen, the Netherlands or for geothermal production in Basel, Strasbourg and recently in Cornwell have shown a significant rise in the number of detected induced events (Reshetnihov et al. 2015; Bardainne et al. 2008; Schmittbuhl et al. 2021; Spetzler and Dost 2017). Early monitoring and accurate location of subsurface production is relevant which became clear in the geothermal project in Pohang, South Korea, that was cancelled after an increase in induced seismicity with a M5.5 main shock (Grigoli et al. 2018).

A variety of hypocenter methods have been suggested in the literature. Lienert et al. (1986) improved the general approach for hypocenter location by Geiger (1912). This method works on single-phase traveltimes and iteratively updates the hypocenter until the residual time can no longer be minimised. Other hypocenter methods focus on the estimation of the source depth by using the traveltime difference between P- and S-phase arrivals per station (Aki and Richards 1980). Pyle et al. (2023) use the S-P arrival time difference at stations near the epicenter to constrain the depth of the event. Lomax (2005), Font et al. (2004), Theunissen et al. (2012) and Spetzler and Dost (2017) used the traveltime difference of P-phases between multiple stations to calculate the hypocenter. The approach by Lomax (2005) (i.e. Non-Lin-Loc, alomax.free.fr/nlloc/) allows to define the error ellipse of the estimated hypocenter. The engine to calculate traveltimes for most of the hypocenter works mentioned in this section is based on some variation of the ray tracing theory which quickly loses validity in relatively complex media (Spetzler et al. 2002). To get around this issue, the Non-Lin-Loc approach allows to calculate traveltime tables for P- and S-wave arrival times with the fast marching method (FMM) (Podvin and LeComte 1991). Smith et al. (2020) show that the validity of the FMM for a 3D complex model for the Groningen region, north-east of the Netherlands, is limited to a distance of around 10 km from the epicenter. Willacy et al. (2019, 2020) carried out a moment tensor inversion (MTI) of induced earthquakes in the Groningen field. The Green's functions for the MTI were calculated with a finite-difference waveform scheme for the 3D complex model. Due to the computational demands of this inversion, the target area for induced earthquakes was initially limited to a 20x20 km^2 area, but later extended to the complete reservoir area. At last, there is the double difference method (also known as HypoDD) (Waldhauser and Ellsworth, 2000;Zhang and Thurber, 2006) which is often used to relocate earthquakes. The idea behind hypoDD is to relate traveltime differences for multiple pairs of nearby events recorded at one station to the relative position of their hypocenters and origin times. Relocation analysis of seismicity by this method often shows clear clustering of repositioned events.

To distinguish between induced and tectonic earthquakes, Dahm et al. (2015) propose a statistical method based on Coulomb stress changes and a rate/state-dependent seismicity model. The authors require that the hypocenter and the uncertainty are known inputs in the evaluation method. Zaliapin and Ben-Zion (2016)

analyse statistical features in large sets of earthquakes to separate between induced and tectonic events. The resulting plots with rescaled time and distance show clusters of events which can be used to indicate the origin of the earthquakes. Tectonic earthquakes tend to have shorter rescaled time and distance due to a regional stress field. Oppositely, induced events group at longer rescaled time and distance are related to localised stress changes which are produced by local injection or extraction.

The detection and location of earthquakes allows to investigate the interior of the Earth. To obtain accurate models of fault systems, geological structures or stress changes over time in the crust or deeper parts of the Earth, geophysics rely on good estimations of the hypocenter location and the uncertainty of earthquakes. That is the reason for this work to as accurately as possible construct a hypocenter method that accounts for proper wavefield propagation in arbitrary velocity models and to obtain precise hypocenters related to the least error range. This paper presents a refined methodology to calculate the hypocenter and associated uncertainty of the earthquake location. The validity of the fast matching method by Podvin and LeComte (1991) for a given velocity profile to calculate P- and S-wave phase times is tested by comparison with finite-difference waveform simulations. In media too complex for the fast marching method to be valid, it is still possible to calculate P- and S-wave arrival times by means of finite-difference or finite-element waveform calculations which allows to account for the wavefield interference of propagating transmitted, reflected, refracted and guided waves. The effect of the choice of phase differences for the hypocenter estimation for the case of (1) only P-S traveltime differences per station, (2) P-wave traveltime difference per two stations and (3) a combination of both is analysed. Synthetic experiments with shallow, intermediate and deep events representative for induced and tectonic seismicity are implemented to investigate which phase difference attribute can provide the smallest hypocenter uncertainty. The refined hypocenter methodology is applied in real case studies of (1) induced seismicity inherent to gas storage in salt diapirs, geothermal production and gas extraction for sites in the Netherlands and (2) tectonic events detected in the border region between the Netherlands, Belgium and Germany.

2 Traveltime tables from finite-difference wavefield simulations

Often traveltime computations are performed with the ray tracing theory (Aki and Richards 1980). The ray theory is derived from the wave equation using a high-frequency approximation implicating that this specific approach can be used in media with large-scale and weak velocity contrasts. Spetzler and Snieder (2004) discuss the validity of the ray theory and show examples of how to compute the traveltime of wavefields with a finite frequency for both transmitted and reflected waves. Spetzler et al. (2002) and Jocker et al. (2006) tested the validity of the ray theory in an ultrasonic waveform experiment. To have the ray theory to actually work properly, one must check the accuracy of a ray-tracer with finite-difference or finite-element waveform simulations. Additionally, the ray theory approach depends on the amount of smoothing imposed on the velocity model to avoid spurious deviated rays. Apart from that, it is tedious to get a ray-tracer to account for the proper transmission, reflection and refraction of a wavefield between two points (Dando et al. 2019). The FMM (Podvin and LeComte 1991) offers another approach to solve the eikonal equation to compute traveltime in more complicated media. The Non-Lin-Loc software Lomax (2005) allows calculating phase traveltimes with FMM. This approach was used by Smith et al. (2020) to compute the arrival times of direct P- and S-waves in a hypocenter analysis of induced earthquakes in the Groningen field, in the north-east of the Netherlands. It is seen in Fig. 4 of Smith et al. (2020) that calculated P-phase from the vertical component of the waveform data is predicted too early for epicentral distances larger than 10 km. For the S-wave arrivals for the horizontal component, the misfit between first arrivals and the horizontal component of the waveforms already starts to deviate at 5 km epicentral distance. The reason for the increasing mismatch between first arrival times and waveforms for increasing distance is in this case due to a thick high-velocity salt formation overlying the gas-bearing reservoir in the structural model. A wavefield propagating along and or in the vicinity of large layer contrasts is very burdensome to model because the wavefront will a combination of a multipath wavefield. The ray theory is too simple to describe the effect of multi-pathing because the conditions for the ray theory are invalid (Spetzler and Snieder 2001).

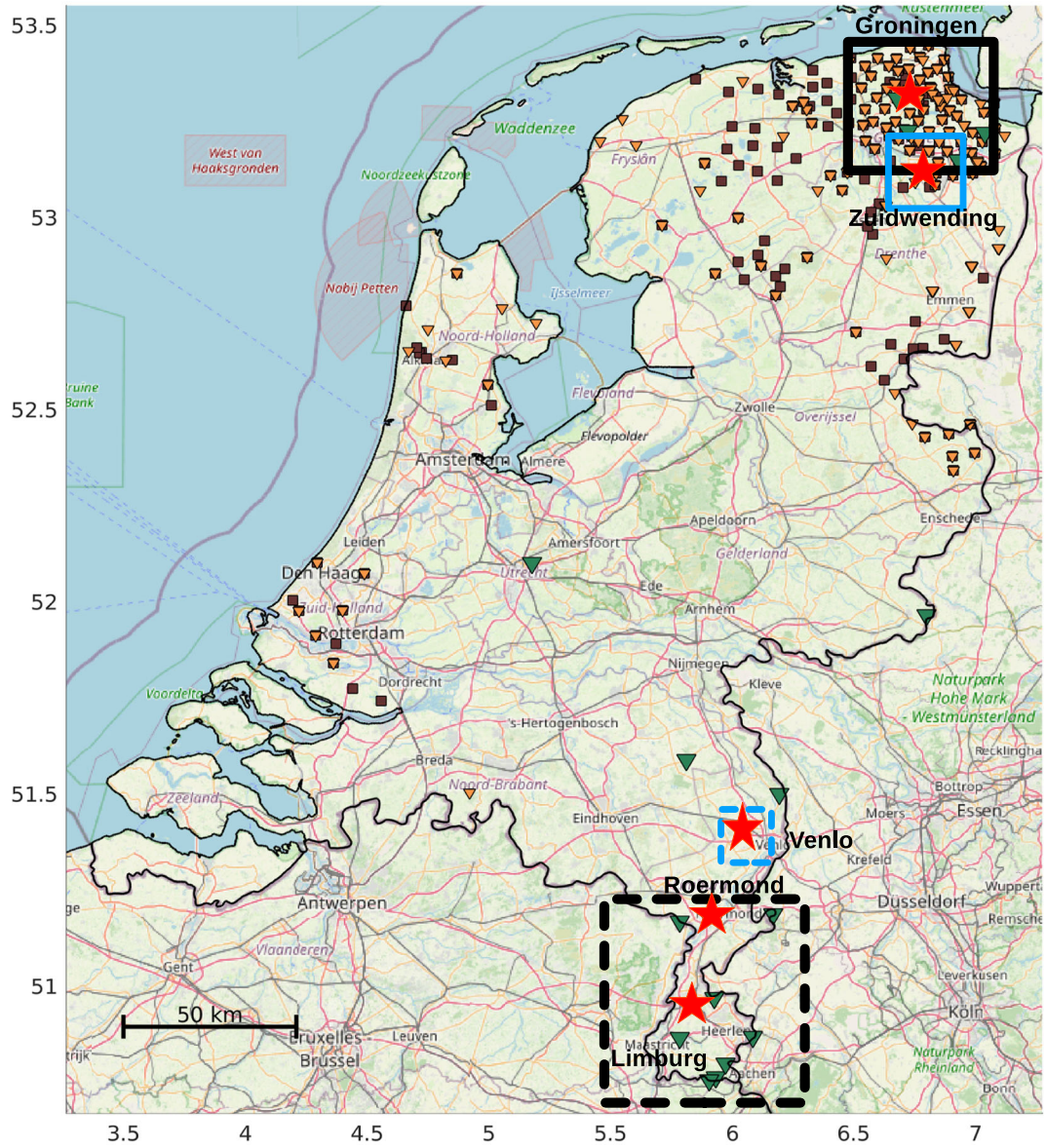

Fig. 1 Seismological network in the Netherlands and locations of induced and tectonic seismicity. The instruments are accelerometers and broadband stations at the surface and borehole stations. Orange triangles denote borehole stations, bordeaux squares are for accelerometers and green triangles illustrate the position of broadband stations (KNMI 2023). The area for induced seismicity due to gas extraction is shown with the black square with solid lines, the location of gas storage in salt diapirs with the blue square with solid line, the geothermal site with the blue square with dashed lines and the area with tectonic events is indicated with the black square with dashed lines. The locations for the induced and tectonic earthquakes in the case studies are plotted with red stars. The map of the Netherlands is from OpenStreetMap (2017)

The finite-difference (FD) waveform method offers a general solution of the wave equation. All wave phenomena are correctly accounted for, and the free surface condition is incorporated in the FD waveform simulations (Robertsson et al. 1994). This is important because of near-surface low velocity layers which have the effect of guiding the wave energy between the surface and shallow layer interfaces. Such a train of propagating wavefields can not adequately be modelled with the ray tracing theory.

We put the FMM and FD modelling schemes to the test for two velocity profiles in the Netherlands. The two velocity profiles are extracted in areas with different geological settings where tectonic and induced earthquakes are detected. Figure 1 shows an illustration of the station network and the regions with known seismicity. Tectonic events occur in the province of Limburg (i.e. the southern part of the Netherlands), while the most part of induced seismicity is recorded in the Groningen gas field (i.e. the north-east of the Netherlands). Figure 2 shows the two P- and S-wave velocity profiles for tectonic earthquakes in Limburg (Profile A) and induced earthquakes in the gas field in Groningen (Profile B). Generally, both locations have increasing P- and S-wave velocities for increasing depth. However, the Groningen gas field is characterised by a thick salt layer between 2 km and 3 km depth and thinner formations of high-velocity anhydrite layers within the salt formation (Dalfsen et al. 2006). The sandstone gas-bearing reservoir below the salt formation has a lower P- and S-wave velocity than the above layers. An illustration of a FD waveform simulation and the picking of first arrivals of recorded waveforms is shown in Fig. 3 for the velocity profile A in Fig. 2. The source depth is 2 km in this example to show the effect of refracted waves at 2 km depth and free surface multiples in the waveform simulation plot. The first arrivals are estimated by kurtosis (Baillard et al. 2014) (i.e. a significant change in frequency content of the wave field defines the phase pick time). A comparison of the waveforms and first arrivals at traces to the distance of 70 km is shown in the lower plot of Fig. 3. For both velocity profiles in Fig. 2, the FMM functionality in the NonLin-Loc software was used to calculate the P- and S-phase times. Next, the P- and S-wave first arrival times for the FMM and FD schemes are compared in Figs. 4 and 5 for the two velocity profiles. Both sets of plots show the traveltime comparison for P- and S-waves for three source depths which are relevant for either tectonic and induced earthquakes. Figure 4 shows that the traveltimes estimated by the FMM and FD schemes are identical for velocity profile A. This is explained

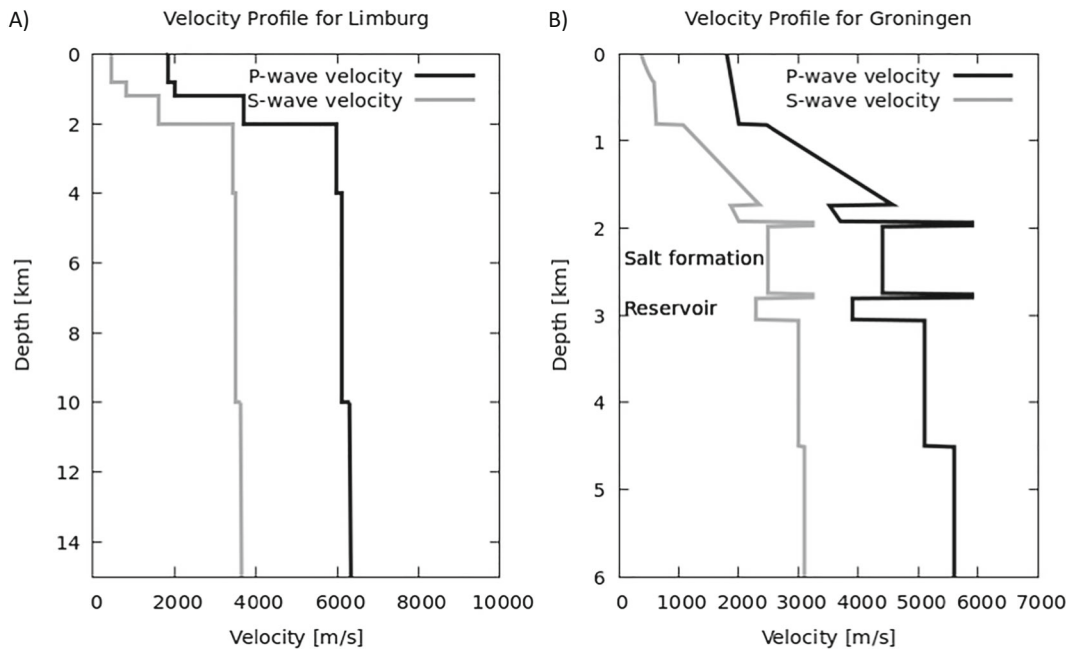

Fig. 2 The P- and S-wave velocity profiles for **A** the southern and **B** north-east of the Netherlands

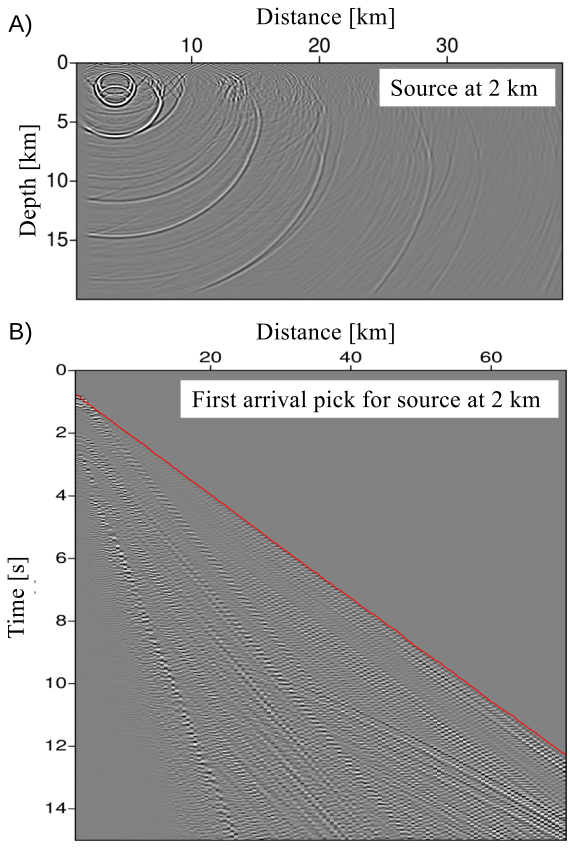

Fig. 3 Example of a finite-difference waveform simulation and first arrival picking by kurtosis (the red line in subplot B). Velocity profile A in Fig. 2 is used in the illustration

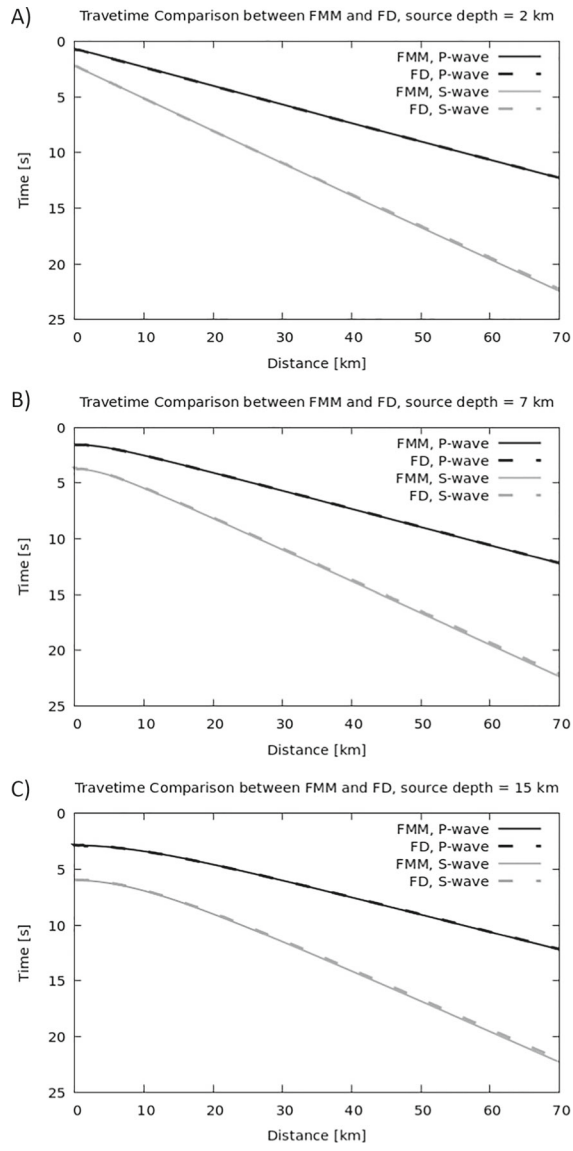

Fig. 4 Picked first arrival times from fast matching method and finite-difference P- and S-waveforms for different source depths at 2 km (**A**), 7 km (**B**) and 15 km (**C**) for the velocity profile A in Fig. 2

by the gradually increasing P- and S-wave velocities for increasing depth that is used in this profile. The results for velocity profile B with the salt formation are very different. Figure 5 shows that the P- and S-wave traveltimes for the FMM method start to deviate from the ones for the FD computations at station distances larger than 3–4 km. Generally, the FMM traveltimes are arriving too early compared to the FD phase times. This observation is in agreement with Smith et al. (2020) though in the example in this paper the breakdown of the FMM methodology happens at shorter distances. The velocity inversion and large velocity contrasts in the salt formation are responsible for the breakdown of the validity of the FMM methodology. The conclusion of the test presented here is that it is important to test the validity of the ray theory or FMM method with FD waveform simulations for a given model before the hypocenter method is applied on field data.

In the remaining part of the paper, traveltime functions of epicentral distance and depth for P- and S-wave arrival times are computed from FD waveform simulations. To reduce the calculation time of FD waveform simulations, the principle of reciprocity (Strutt and Rayleigh, 1926;Aki and Richards, 1980) is applied to interchange source and receiver positions. This means that the receiver position near the surface of the model is defined as the source point for the wavefield. The

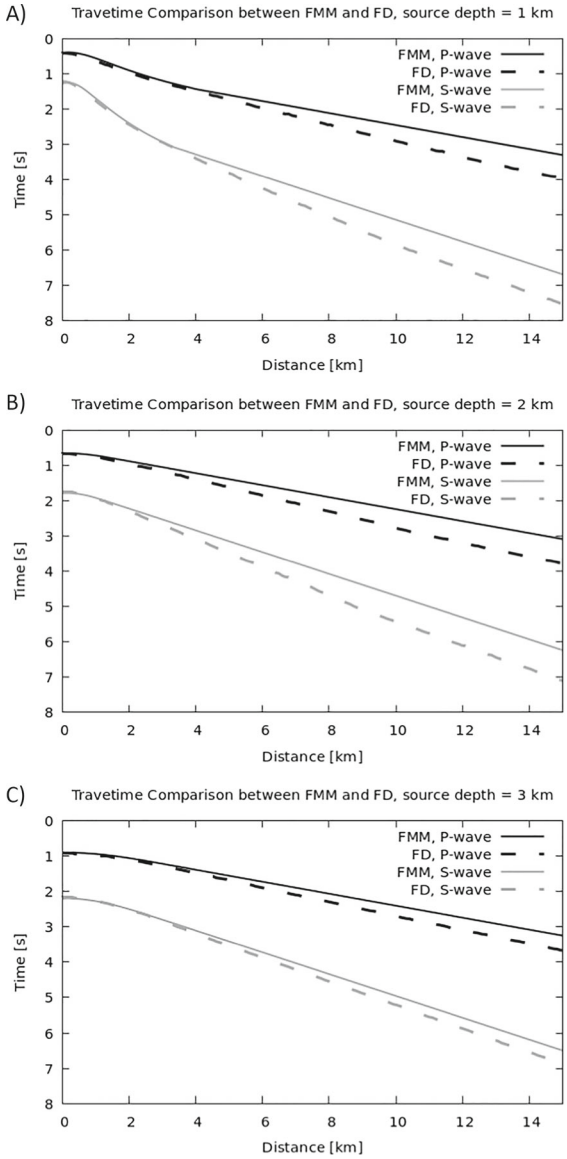

Fig. 5 Picked first arrival times from fast matching method and finite-difference P- and S-waveforms for source depths at 1 km (**A**), 2 km (**B**) and 3 km (**C**) for the velocity profile B in Fig. 2

2D model is covered with a stack of horizontal arrays with receiver points at which the horizontal and vertical component of the propagating wavefield is computed. The first arrival times of the calculated waveforms are estimated by kurtosis (Baillard et al. 2014). Finally, the traveltime tables for P- and S-waves are constructed by combining the traveltime curves for the subsurface horizontal arrays.

3 Methodology for hypocenter and uncertainty estimation

A general methodology to estimate the hypocenter of an earthquake is to find the extremum point of the posterior probability distribution (PPD) (Aki and Richards, 1980;Tarantola, 1987). For traveltime data with normally distributed errors, the PPD is expressed as

$$\sigma(\mathbf{r}) = k \exp\left(-\frac{1}{2}\left[d^{calc}(\mathbf{r}) - d^{obs}\right]^t C_d^{-1}\left[d^{calc}(\mathbf{r}) - d^{obs}\right]\right), \quad (1)$$

where the superscript t is the transpose of the vector difference and the vectors d^{obs} and d^{calc} consist of observed and calculated traveltime data, respectively. The PPD $\sigma(\mathbf{r})$ is computed for a 3D distribution of possible hypocenter locations ($\mathbf{r}$). The constant k is calculated by normalising the PPD to a total probability of one. For every trial hypocenter position ($\mathbf{r}$), the difference term $[d^{calc}(\mathbf{r}) - d^{obs}]$ is computed. The data covariance matrix C_d depends on the chosen data attribute and the timing errors originating from modelling uncertainties, instrumentation and phase picking. The data covariance matrix is calculated from

$$C_d = AC_nA^t, \quad (2)$$

which is a general formulation for the transformation of any Cartesian covariance matrix (Solar and Chin 1985). Matrix A describes how the combination of phase difference attributes is used and relates the data noise vector d to the general noise vector N through $d = AN$ (Tarantola 1987). The noise vector for stations with P- and S-wave traveltime picks is given by

$$N = \begin{pmatrix} \sigma_s^2 \\ \vdots \\ \sigma_p^2 \end{pmatrix}, \quad (3)$$

while the corresponding noise covariance matrix C_n is defined by

$$C_n = \begin{pmatrix} \sigma_s^2 & \cdots & 0 \\ \vdots & \ddots & \vdots \\ 0 & \cdots & \sigma_p^2 \end{pmatrix}. \quad (4)$$

The variances for the P- and S-wave phase attribute are denoted by σ_p^2 and σ_s^2, respectively. These variances describe the uncertainty that exists in the P-wave and S-wave phase picks.

P- and S-wave traveltimes can be used in several ways in a hypocenter analysis. A schematic of the application of phase times for P- and S-waves is illustrated in Fig. 6. It takes a certain time for a seismic wave to propagate from source to station. The arrival times of the P- and S-wave arrivals are recorded. The hypocenter estimation of an earthquake can be based on (A) the difference in P- and S-wave traveltimes per station, (B) the difference in P-wave traveltimes between two stations or (C) a combination of both differences in traveltimes. In this paper, the three ways of using the phase difference attributes in Fig. 6 are denoted P-S mode, P-EDT mode and P-S and P-EDT mode. The matrix A in expression (2) is constructed accordingly to the chosen phase difference mode.

Let a seismic experiment have three stations. The noise covariance matrix C_n in Eq. 4 is a 6x6 matrix with the diagonal first filled with the variances for S-wave traveltimes succeeded by the variance for the P-wave traveltimes. For the P-S mode, the matrix A has the form

$$A = \begin{pmatrix} 1 & 0 & 0 & -1 & 0 & 0 \\ 0 & 1 & 0 & 0 & -1 & 0 \\ 0 & 0 & 1 & 0 & 0 & -1 \end{pmatrix}. \tag{5}$$

and the data covariance matrix is calculated from Eq. 2 resulting in

$$C_d = \begin{pmatrix} \sigma_s^2 + \sigma_p^2 & 0 & 0 \\ 0 & \sigma_s^2 + \sigma_p^2 & 0 \\ 0 & 0 & \sigma_s^2 + \sigma_p^2 \end{pmatrix}. \tag{6}$$

For the P-EDT mode where P-wave traveltime differences between pairs of stations are used, only the right side block of the matrix A is build. For the case of three stations, the P-traveltime difference between the one station and the two next stations is written in two rows as

$$A = \begin{pmatrix} 0 & 0 & 0 & -1 & 1 & 0 \\ 0 & 0 & 0 & -1 & 0 & 1 \end{pmatrix}. \tag{7}$$

and the data covariance matrix is calculated from Eq. 2 giving

$$C_d = \sigma_p^2 \begin{pmatrix} 2 & 1 \\ 1 & 2 \end{pmatrix}. \tag{8}$$

In the P-S and P-EDT mode where differences between P- and S-wave traveltimes per station and between P-wave travetimes between two stations are

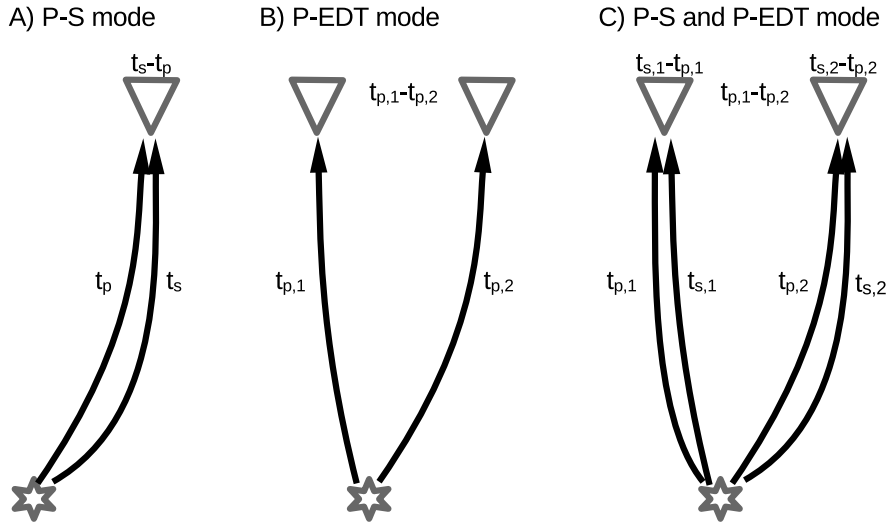

Fig. 6 Schematics of three ways to use P- and S-wave phase arrivals in hypocenter estimation. **A** P-S mode: The difference between P- and S- wave arrival times per station. **B** P-EDT: The difference between P-wave phase times between pairs of stations. **C** P-S + P-EDT mode: A combination of the two previous phase differences

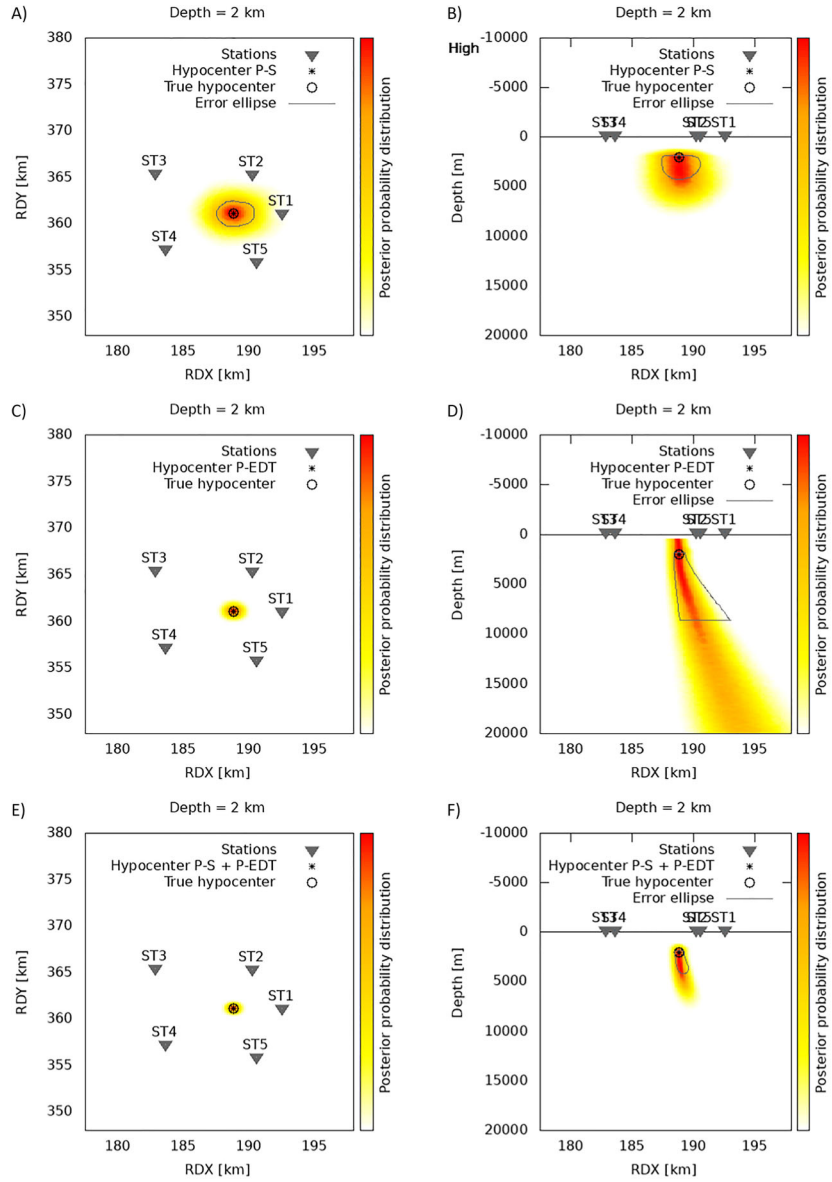

Fig. 7 Hypocenter analysis of a synthetic earthquake at 2 km depth and an average station distance at 5 km. The format of the plot are three rows with the hypocenter results first for the P-S mode, then the P-EDT mode and finally the combined P-S and P-EDT mode. The representation of the hypocenter solution is projected onto a horizontal and vertical cross-section which are plotted in the respectively first and second columns. The estimated and true hypocenters are shown with the star and circle, respectively. The 95 percentile volume of the posterior probability distribution for the estimated hypocenter is illustrated with orange-yellow colours (yellow for low values and orange for high values of the normalised PPD). The error ellipse for the first standard deviation of the posterior probability distribution is shown with a thin gray line. If the area for the 95 percentile posterior probability distribution is small in a plot, the error ellipse will not be clearly visible and is omitted. The horizontal and vertical cross-section is shown for all three phase arrival modes. P-S mode: **A** and **B**. P-EDT mode: **C** and **D**. P-S + P-EDT mode: **E** and **F**

combined, the matrix A is written as

$$A = \begin{pmatrix} 1 & 0 & 0 & -1 & 0 & 0 \\ 0 & 1 & 0 & 0 & -1 & 0 \\ 0 & 0 & 1 & 0 & 0 & -1 \\ 0 & 0 & 0 & -1 & 1 & 0 \\ 0 & 0 & 0 & -1 & 0 & 1 \end{pmatrix}. \tag{9}$$

and the data covariance matrix is calculated from Eq. 2 with the result

$$C_d = \begin{pmatrix} \sigma_s^2 + \sigma_p^2 & 0 & 0 & \sigma_p^2 & \sigma_p^2 \\ 0 & \sigma_s^2 + \sigma_p^2 & 0 & -\sigma_p^2 & 0 \\ 0 & 0 & \sigma_s^2 + \sigma_p^2 & 0 & -\sigma_p^2 \\ \sigma_p^2 & -\sigma_p^2 & 0 & 2\sigma_p^2 & \sigma_p^2 \\ \sigma_p^2 & 0 & -\sigma_p^2 & \sigma_p^2 & 2\sigma_p^2 \end{pmatrix}. \tag{10}$$

The PPD in expression (1) requires that the inverse of the data covariance matrix C_d exists. This means that the data covariance matrices in Eqs. 6, 8 and 10 must have a non-zero determinant. For the P-S mode in Eq. 6, it is trivial. However, for the station configuration matrices in Eqs. 8 and 10, the P-wave traveltime difference between the second and third station is omitted since it turns out that this last traveltime difference between two stations is linearly dependent on the two traveltime differences between the first station and the other stations. Generally for a seismological network with n-stations, the station configuration matrix for the part of the P-EDT mode will be constructed for one station and the remaining n-1 stations in order to calculate the inverse of the data covariance matrix. There is therefore no need to use a regularisation condition to calculate the inverse of the data covariance matrix in Eq. 2 for any of the three phase difference modes which is used in the objective function in expression (1).

At last, the procedure to estimate the hypocenter and uncertainty of an earthquake is explained. The hypocenter is estimated in a grid search optimisation of expression (1) for the choice of phase difference mode. The error ellipse is defined as one standard deviation of the posterior probability distribution in each direction. According to Wang et al. (2015), the first standard deviation is obtained by dividing the 95 percentile of a 3D distribution by 2.795. Pyle et al. (2023) define as well the 95 percentile as the boundary for the error ellipse. The complete hypocenter solution will be a point for the epicenter (x, y) and depth (z) of the event surrounded by an uncertainty volume.

4 Synthetic example

The synthetic example is designed to simulate earthquakes at different depths. Three cases with source depths at 2, 7 and 15 km are analysed. The velocity profile A in Fig. 2 is used in the example. The effect of the station distance and distribution to the source is investigated as well. Bear in mind that the possibilities of station configurations are endless. We want to keep the synthetic example simple and have therefore placed 5 stations around the source point. The station distance is uniformly distributed with an average distance of 5 km or 15 km which corresponds to representative distances in local and regional station networks. The azimuthal distribution is unaltered in the synthetic experiment. Examples of uneven station configurations can be found in the case studies of induced and tectonic events in the Netherlands in the next section. An addition of different noise components to data is not meaningful since the variance for the P- and S-wave phases is already defined in the noise covariance matrix in Eq. 4. The traveltimes for P- and S-wave picks are extracted from the finite-difference traveltime tables to calculate the "true" input data for each source-station combination. The hypocenter and error ellipse are estimated for all three phase difference modes (i.e. the P-S mode, P-EDT mode and P-S and P-EDT mode). Representative values for the uncertainty of P- and S-waves are set to σ_p = 137 ms and σ_s = 248 ms which have been estimated in a regional seismic network in the north of the Netherlands (Table 1). The network types in the Netherlands are discussed in the next section.

The results for the hypocenter analysis are presented in Figs. 7, 8, 9 and 10 for the average station distance at 5 km and 15 km, respectively. An inspection of the hypocenter plots for the average station distance at 5 km reveals that the original hypocenter is perfectly reproduced by the inversion methodology. This is simply a demonstration that the forward and inverse problem is correctly implemented. The most likely hypocenter is only part of the complete solution. The uncertainty of the hypocenter solution must be addressed, too. Generally, it is observed in the plots that the smallest uncertainty is obtained with the combined P-S and P-EDT mode inversion. The P-S mode inversion tends to have

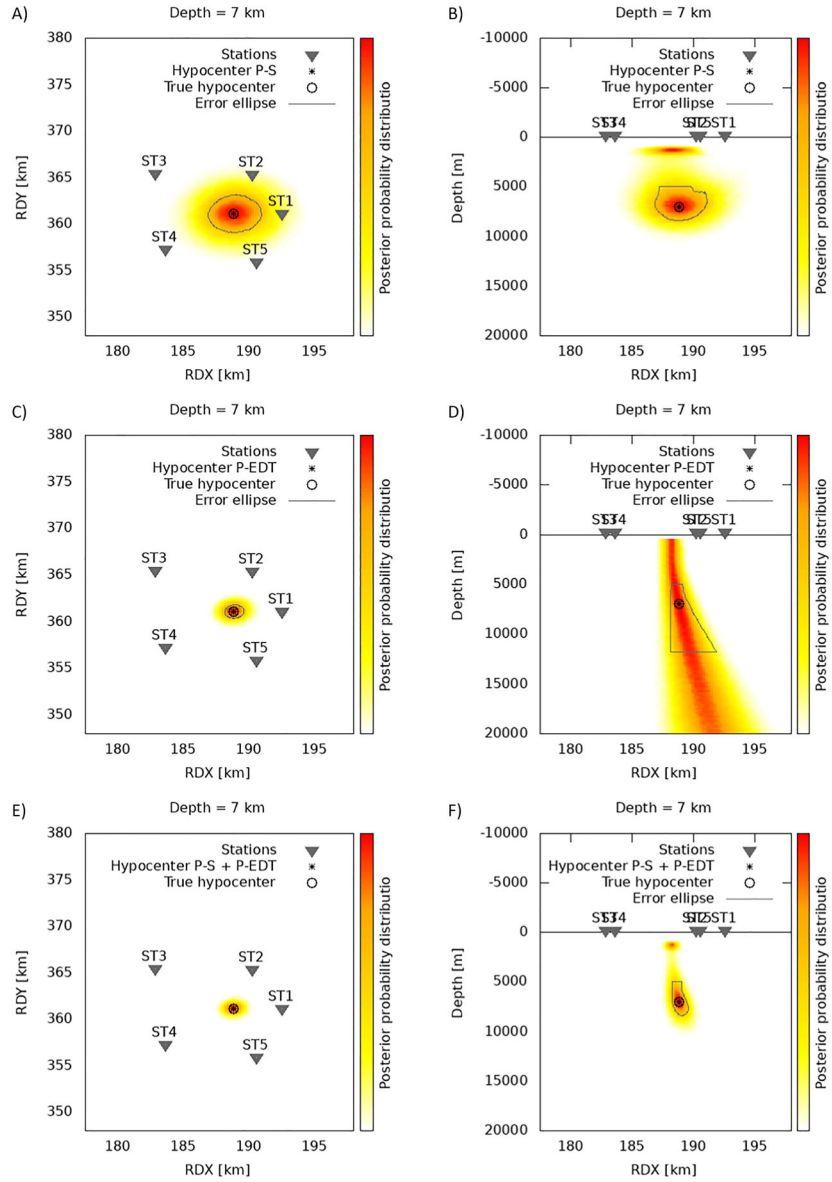

Fig. 8 Hypocenter analysis of a synthetic earthquake at 7 km depth and an average station distance at 5 km. The horizontal and vertical cross-section is shown for all three phase arrival modes. P-S mode: **A** and **B**. P-EDT mode: **C** and **D**. P-S + P-EDT mode: **E** and **F**. The format and symbols are the same as in Fig. 7

the largest uncertainty in the epicenter, while the uncertainty area is smaller for the depth estimate. For the P-EDT mode inversion, the uncertainty in the epicenter is smaller but the uncertainty in depth is cone shaped with increasing width for deeper structures. The combined P-S and P-EDT mode inversion benefits from the best of the two individual approaches and provides a hypocenter solution with the smallest uncertainty in epicenter and depth. This latter point is demonstrated in Fig. 10 for the average station distance at 15 km.

Another remarkable observation is the rather large vertical extension of the uncertainty of the hypocenter solution for shallow-to-intermediate source depths in Figs. 7, 8 and 10. The reason for this is the slowly

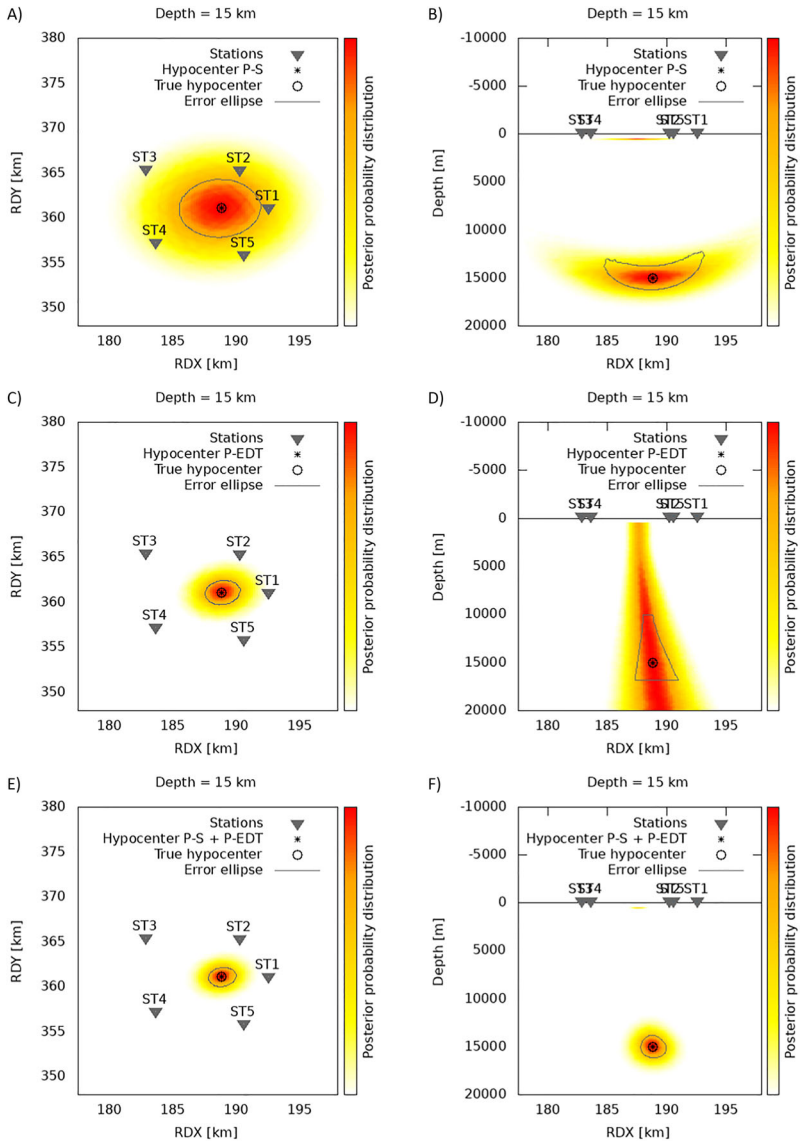

Fig. 9 Hypocenter analysis of a synthetic earthquake at 15 km depth and an average station distance at 5 km. The horizontal and vertical cross-section is shown for all three phase arrival modes. P-S mode: **A** and **B**. P-EDT mode: **C** and **D**. P-S + P-EDT mode: **E** and **F**. The format and symbols are the same as in Fig. 7

Table 1 The uncertainty (i.e. the first standard deviation) in the P- and S-phase traveltimes for different networks in the Netherlands

Area	σ_p [ms]	σ_s [ms]	Network type
North Netherlands	137	248	Regional
South Netherlands	200	300	Regional
Groningen	50	75	Regional
Zuidwending	20	25	Local
Venlo	108	120	Local

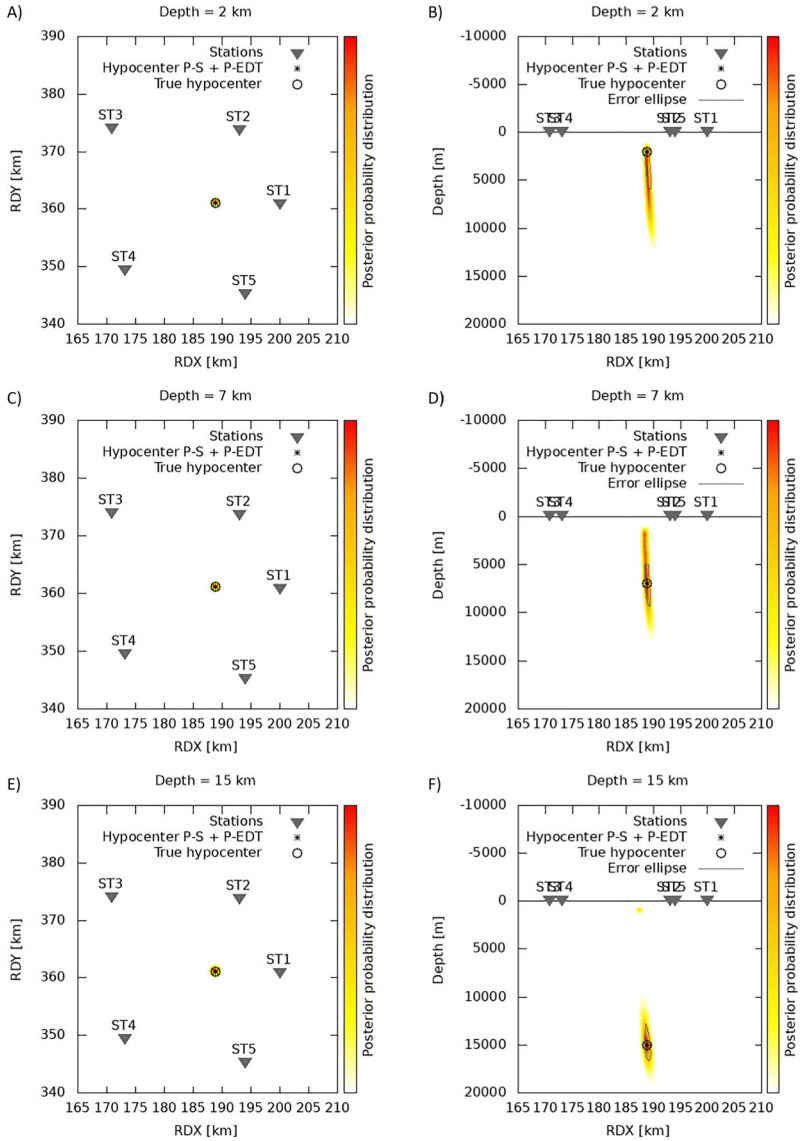

Fig. 10 Hypocenter analysis of a synthetic earthquake at several depths and an average station distance at 15 km for only the P-S and P-EDT mode. The horizontal and vertical cross-section is shown for all three phase arrival modes. 2 km depth: **A** and **B**. 7 km depth: **C** and **D**. 15 km depth: **E** and **F**. The format and symbols are the same as in Fig. 7

Table 2 Hypocenter solution from different affiliations for the induced event in the geothermal field near Venlo

Affiliation	X [m]	Y [m]	Depth [m]
This paper	204,546 ± 190	380,305 ± 230	2000 ± 360
Q-con	∼ 204,042	∼ 380,050	∼ 2400
KNMI	208,497 ± 4000	379,488 ± 4000	1000 (fixed)

The uncertainty for the hypocenter solution from Q-con is not given in Vörös and Baisch (2022). The coordinates are given in the Dutch RD (in Dutch: Rijksdriehoeksstelsel, http://www.kadaster.nl/web/Themas/Registraties/Rijksdriehoeksmeting/Rijksdriehoeksstelsel.htm) coordinate system

increasing velocities for increasing depth from 2 km in profile A of Fig. 2. Given a station distance, traveltimes for either P- or S-waves can have comparable values at various depths which will result in a multitude of possible hypocenter solutions, hence extending the uncertainty area.

Another question to be addressed is the effect of the station distance on the hypocenter uncertainty. Notice that the plots for the hypocenter solutions for the average station distance at 5 km and 15 km do not have the same lateral scale because it would be difficult to produce clear plots with identical spatial ranges. A close examination of the uncertainty ellipses in Figs. 7, 8, 9 and 10 does not favour either short nor long station distance. In the synthetic experiment, the effect of station distance is irrelevant since the detectability of good phase picks is unlimited. However, in a hypocenter analysis of real earthquakes, the station distance is of great importance due to indeed limited detectability of P- and S-waves. The signal detectability depends on the quality of the network, radiation patterns of the seismic sources, attenuation effects and the magnitude of the event. The case studies of hypocenter analysis of induced and tectonic earthquakes in the next section provide more information about the effect of the station distance in different types of networks.

Finally, the effect of a poor azimuthal distribution of stations has been investigated. The synthetic experiment is set up with 5 stations around the source, the station distance is uniformly distributed with an average distance of 15 km, but this time, a range of azimuthal gaps from 72° to 350 ° is introduced. The hypocenter inversion for the combined P-S and P-EDT phase attribute is carried out. The results are presented as the horizontal and vertical uncertainty of the hypocenter as function of azimuthal gap. Figure 11 shows that the horizontal uncertainty is much affected by an increase in azimuthal gap while the vertical uncertainty remains more or less constant. The synthetic experiment indicates that the uncertainty of a hypocenter will remain limited even for an azimuthal gap of 200–250 degrees. The case study of hypocenter analysis of tectonic events with a large azimuthal gap shows indeed that the error ellipse can be small enough to have a well-defined range for the source location.

A Python program is provided as supplementary information to give the reader the opportunity to test the effect of the choice of phase difference mode (i.e. P-S, P-EDT, P-S and P-EDT). To simplify the program code, the example is limited to a 2D constant velocity model. The short note "Python_instructions.pdf" in the supplementary information explains how to set the parameters before executing the program.

5 Hypocenter solution of events in the Netherlands

The hypocenter methodology is tested for several case studies of induced and tectonic earthquakes. The cause for the induced seismicity is either gas storage in salt diapirs, geothermal production or gas extraction. These are subsurface activities found abundantly in the Netherlands. The examples with tectonic events are from a region in the south of the Netherlands known for natural seismicity. Available local velocity profiles are incorporated in each separate hypocenter analysis except for the source location estimation of the tectonic events where profile A in Fig. 2 is used. Figure 1 illustrates with coloured squares the areas of induced and tectonic seismicity in the Netherlands and the current national seismological network (KNMI 2023). The instrumentation is a mixture of surface accelerometers, broadband stations and borehole geophones. Most

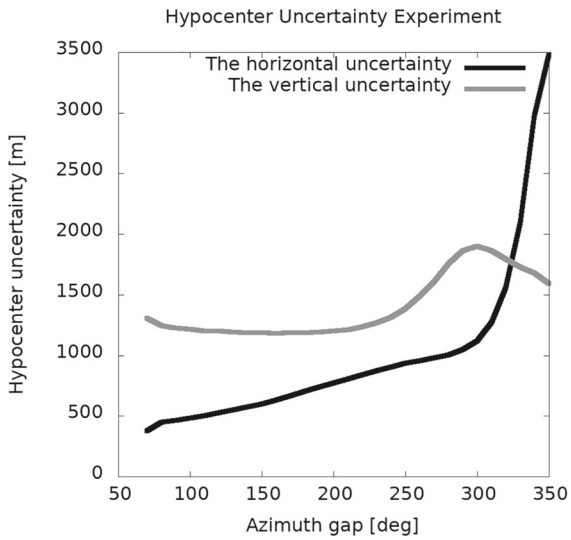

Fig. 11 Estimation of the hypocenter uncertainty in a synthetic experiment with a range of azimuthal gaps between 72 and 350 degrees. The source depth is 15 km, and the average station distance is 15 km

instruments have been added in the past 10 years due to (1) a rise in induced seismicity in the Groningen gas field, the north-east of the Netherlands, (2) recent developments in geothermal production near the Hague, (3) gas storage in depleted gas fields and (4) wastewater disposal into a depleted gas/oil reservoir. There are few broadband stations in the north and west of the Netherlands. The majority of broadband stations have been installed in south-east of the Netherlands in order to detect tectonic earthquakes. Besides the national network, several local networks are installed on gas storage sites, small producing gas fields and geothermal production sites. For these locations, local velocity models are available from well-logs provided by contractors. Traveltime tables are computed with the finite-difference waveform simulations for the local velocity models.

Figure 12 shows an example of recorded waveforms for an induced event in Groningen and a tectonic earthquake in Limburg. These two examples are used in the case study of relocated hypocenters further in the article. The impact of the dense network to detect induced earthquakes in the Groningen field is illustrated by the short epicentral distance in waveform plot A. In the south of the Netherlands, the sparse broadband station network result in long epicentral distances which is seen in the waveform plot B. Generally, the waveform data show clear P-phase arrivals, whereas the later S-phase arrivals are still visible. The signal-to-noise ratio is good enough (i.e. >3) to pick phases in the plotted waveforms which is a general characteristics of many events detected in the Dutch seismic network in the Netherlands.

The uncertainties for P- and S-waves in picked traveltimes (i.e. σ_p and σ_s) in Eq. 4 have been determined for the northern part, southern part and the Groningen region of the Dutch national station network and for the local stations on gas storage and geothermal production settings. Many event detections are available in the national network (see the KNMI earthquake catalogues for induced and tectonic events, www.knmi.nl). The uncertainties for P- and S-waves were obtained in a statistical analysis of the deviation of picked arrival times with respect to traveltimes based on a reference velocity model. On the other hand, there are not many recorded events in the local networks. In that case, the estimate relies on an expert opinion and a calculation of the standard deviation of a limited number of residual

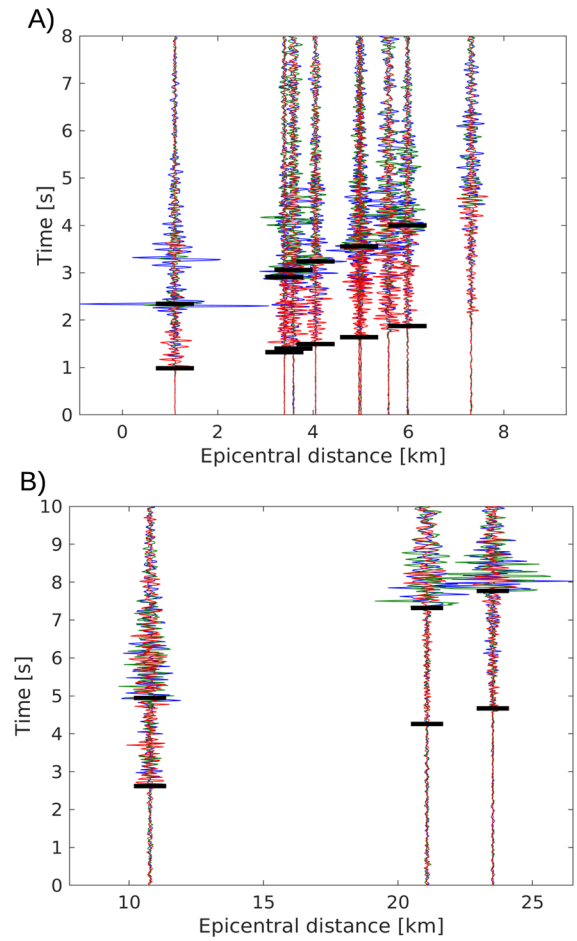

Fig. 12 Waveform plots of **A** a M0.6 induced event on November 28, 2021, in Groningen, north-east of the Netherlands and **B** a M1.2 tectonic event on November 2, 2017, in the south of the Netherlands (source: www.knmi.nl). The colour codes for the waveform data are red, blue and green for the vertical, radial and transversal components. The waveforms are band-passed filtered between 3 and 18 Hz

traveltimes for P- and S- waves. The uncertainties for P- and S-waves in the individual network branches are given in Table 1. The smallest uncertainties are found for the local network on the gas storage site in Zuidwending. This network is state-of-the art with borehole stations with two instruments at about 60 m and 90 m depth (source: the contractor). The noise conditions (generally signal-to-noise level $>$ 3–4) are good enough to be able to pick both P- and S-wave phases in the recorded waveforms (not shown in this paper). The local network at the geothermal production site near Venlo consists of surface stations. Consequently, the noise level in the measurements is accordingly higher

causing greater values for the P- and S-wave uncertainties. For the national network branches, the uncertainties for P- and S-waves are smallest for Groningen which is characterised by short station distances in the order of 3–4 km. Station distances increase for the network part in the north of the Netherlands and are much longer (i.e. 20–50 km) for instruments in the south of the Netherlands. This is reflected in the increment in the uncertainty in P- and S-waves.

Several case studies compare the hypocenter solution obtained in this paper with the hypocenter location in the KNMI official earthquake catalogue (www.knmi.nl/kennis-en-datacentrum/dataset/aardbevingscatalogus). To help understand, the difference between the two hypocenters, a short note has been prepared in the supplementary information to explain the method in the KNMI daily operations. The operational procedure remains fixed for the time being. Likewise, the official earthquake catalogues for induced and tectonic events in the Netherlands will remain unchanged. Instead, refined locations will be available as a research earthquake catalogue.

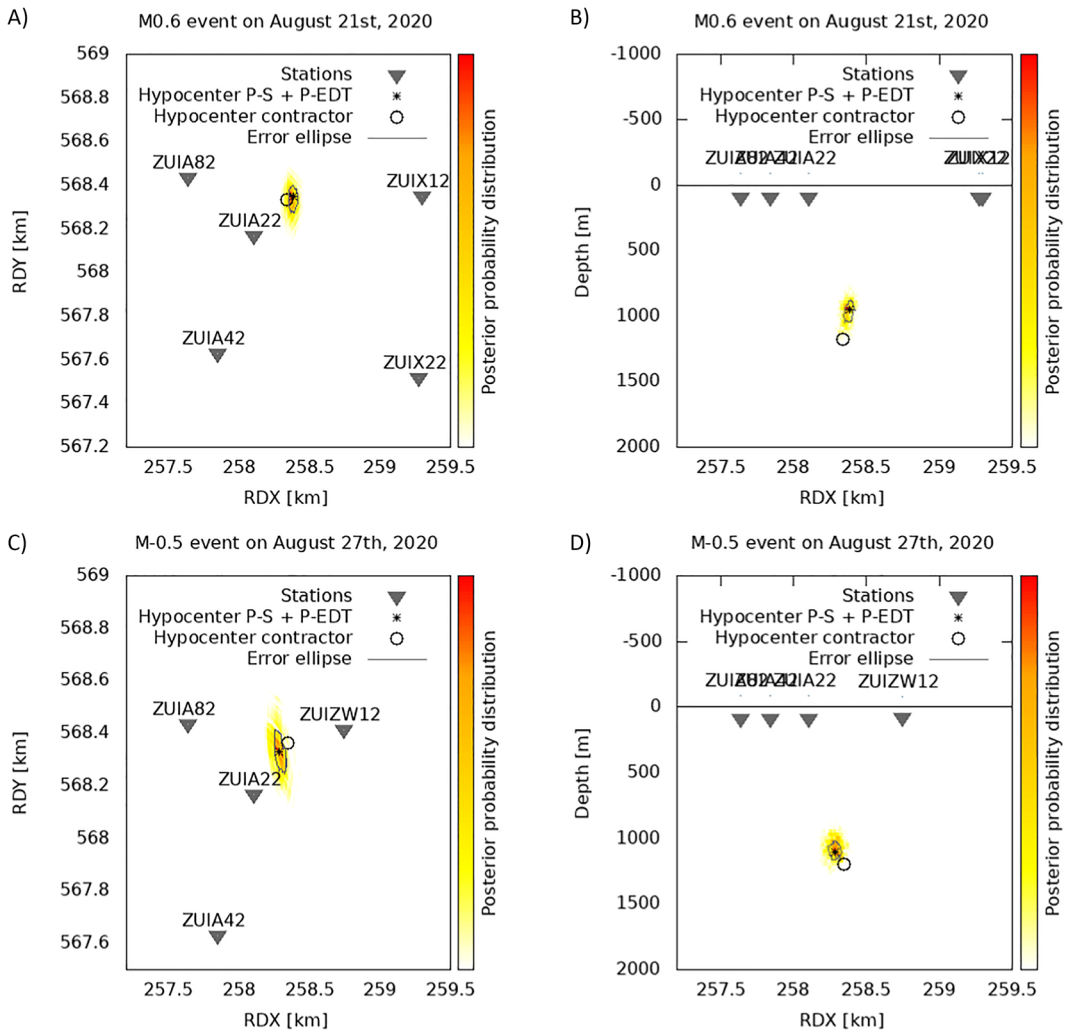

Fig. 13 Hypocenter analysis of two shallow induced earthquakes due to gas storage in a salt cavern. **A** and **B** are the horizontal and vertical cross-sections of a M0.6 event. **C** and **D** are the two cross-sections of a M−0.5 event. The format and symbols are the same as in Fig. 7

5.1 Induced events

The subsurface of northern Netherlands is characterised by a thick formation of salt, geologically known as the Zechstein layer (Dalfsen et al. 2006). In the Groningen region, the Zechstein layer is 1 km thick and local salt diapirs have pushed upward to 1 km below or even closer to the surface. Such locations are favourable for gas storage. On one location, 6 salt caverns with volumes, 300–400 m height by 50–80 m width are situated below 1 km depth and are used as gas depots for usage during winter. In August 2020, two events with a magnitude 0.6 and −0.5 were recorded by the contractor who is monitoring the production area for induced seismicity. For both events, clear waveforms were recorded at 4–6 borehole stations and P- and S-phase times were picked by the contractor and further used in this hypocenter analysis The contractor's report is confidential, but the waveforms can be downloaded from the KNMI data portal (www.knmi.nl/kennis-en-datacentrum/dataset/seismische-en-akoestische-data-tools). The relocated hypocenters using the P-S and P-EDT mode for the two events are presented in Fig. 13. The events have a similar hypocenter. The epicenters and depth estimates are well-defined with a small spatial uncertainty. The contractor performed an independent hypocenter analysis based on the same velocity profile and a classical P-S mode approach. Both analyses show similar results. The cause of the induced events according to the contractor is a rock fall at the edge of the cavity in the salt diapir.

There is an increasing focus on geothermal energy as part of the transition from fossil fuels to re-useable and climate friendly energy sources. Often, geothermal plants are built near greenhouses to supply heat during wintertime. In one case, a M2.0 event was detected at a site with geothermal production near the city Venlo, the south-east of the Netherlands (Vörös and Baisch 2022). The event was large enough to be felt locally by few people and was recorded at the five surface stations (i.e. K01-K05) of the local network. P- and S-wave arrival times were picked, and the hypocenter was estimated using the P-S and P-EDT mode. The KNMI report (Spetzler et al. 2018) includes a plot of the waveform data and a section with an investigation of the local velocity profile. Figure 14 shows the relocated hypocenter and uncertainty volume (K05 is further away from the wells and not seen in the plots). In addition, a quantitative comparison of the three hypocenters for the induced event is given in Table 2. The hypocenter is located at about 2.0 km depth, close to the doublet system. The wells CAL 01-05 are indicated by gray lines in Fig. 14, and they are extending to 1.6 km and 2.4 km below the surface. The estimated hypocenter depth by the contractor Q-con is about 2.4 km although no uncertainty in the hypocenter is provided in Vörös and Baisch (2022). Q-con used well perforation shots to

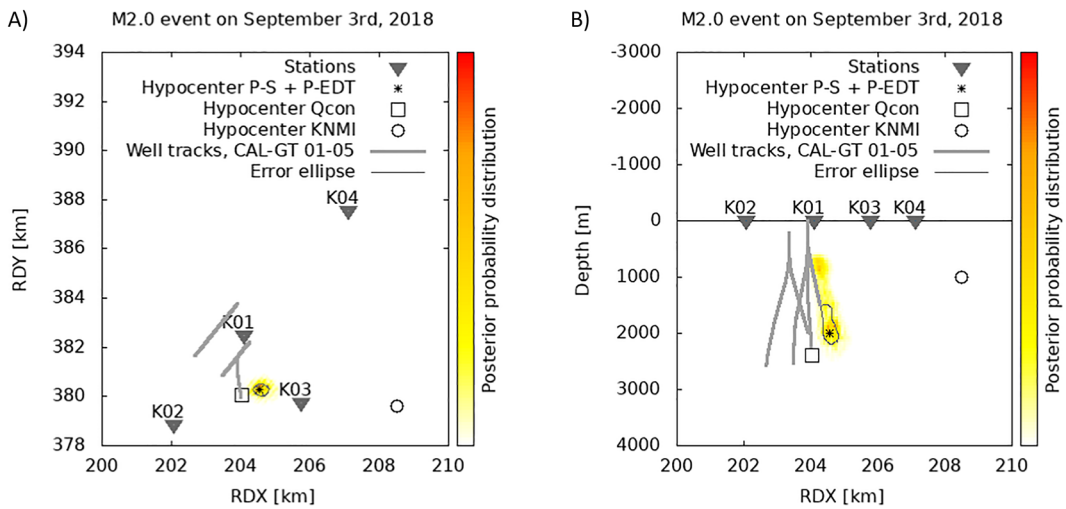

Fig. 14 Hypocenter analysis of shallow induced earthquake due to geothermal production. **A** and **B** are the horizontal and vertical cross-sections of a M2.0 event. The format and symbols are the same as in Fig. 7

calibrate the inverse velocity difference $(1/V_s - 1/V_p)$ and then determined the hypocenter solution which was found to be located between the wells of the doublet system. The presented hypocenter from this paper and the Q-con source solution are close considering the uncertainty range of the applied hypocenter methods. The KNMI hypocenter solution is calculated from distal stations in the national network and the Seiscomp software, resulting in a hypocenter solution far from the more likely location determined in this paper and by Q-con.

The last case study to discuss in this subsection is induced seismicity due to the extraction of gas. The gas is produced from the Groningen gas field which has resulted in many small events and the recorded maximum magnitude is 3.6, (deJager and Visser 2017). The velocity profile B in Fig. 2 shows an example of the structure of the overburden and gas-bearing reservoir. The lateral extension of the gas reservoir is almost 25x40 km^2. The first induced event was recorded in 1991. The induced seismicity steadily increased due to an increase in production of gas in following years (Dost et al. 2017). Spetzler and Dost (2017), Willacy et al. (2019, 2020) and Smith et al. (2020) made estimates of the hypocenter of induced events in Groningen based on different approaches. All three studies show that the events predominantly occur at reservoir level. Figure 15 presents the result of the hypocenter analysis

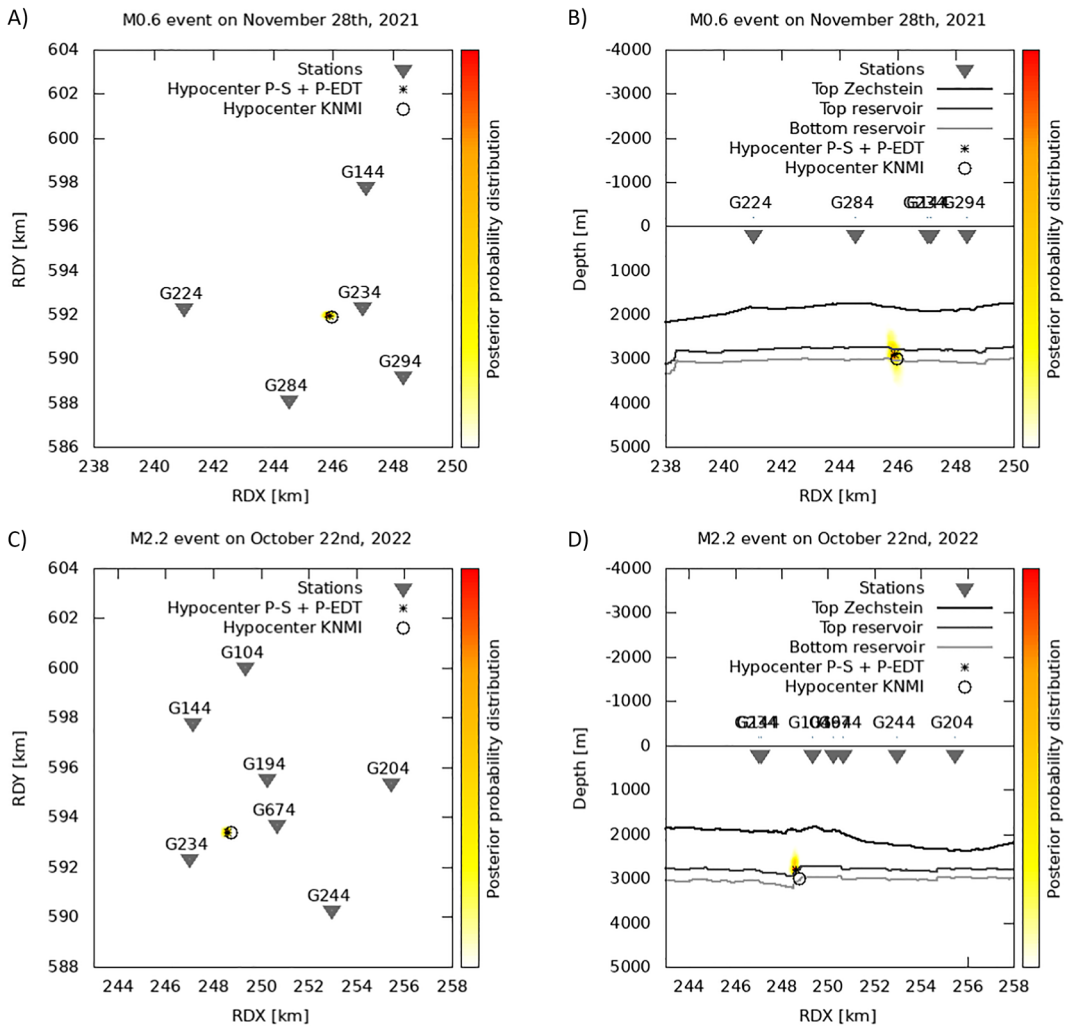

Fig. 15 Hypocenter analysis of shallow induced earthquake due to gas extraction. **A** and **B** are the horizontal and vertical cross-sections of a M0.6 event. **C** and **D** are the two cross-sections of a M2.2 event. The format and symbols are the same as in Fig. 7

of two events: a M0.6 in 2021 and a M2.2 event in 2022. The azimuth distribution of stations is almost uniform around the hypocenters, and the maximum azimuthal gap is less than 90 deg and station distances are below 7 km. A comparison with the hypocenter published by the KNMI (source: Induced earthquake catalogue on www.knmi.nl) and the relocated hypocenter reveals a similar outcome. The depth in the KNMI hypocenter is by default set to 3 km without defining the error. The top of the Zechstein layer and the vertical extension of the gas reservoir (extracted from the 3D elastic model for the Groningen field, Romijn (2017)) is indicated in the cross-section with the hypocenter depth in Fig. 15. The estimated hypocenter depths for both events using the P-S and P-EDT mode presented in this paper are between 2900 and 3000 m (± 200 m), indicating that they are confined within the reservoir. The hypocenters are likewise well-defined near faults which is most clear in the cross-section plot for the M2.2 event. The error ellipse slightly extends into the Zechstein layer above and the Carboniferous layer below the reservoir. The QC-reports for the two events estimated by Willacy et al. (2020) published on www.namplatform.nl show similar hypocenters and error ellipses.

5.2 Tectonic events

The border region between the Netherlands, Germany and Belgium is well-known for natural seismicity due to active faulting in the Ruhr Valley Graben (Paulssen et al. 1992). The largest event recorded in this region is the M5.8 event on April 13, 1992, near Roermond, the Netherlands. The earthquake was widely felt and due to a long duration caused much structural damage. Large magnitude events (M > 4) do not take place very often. The recurrence of a large magnitude earthquake in the area is several centuries (Vanneste et al. 2013; Camelbeeck et al. 2020). On the other hand, many small magnitude earthquakes are detected by the broadband stations every year. These small tectonic events are often not felt due to the deep hypocenters. The velocity profiles used to calculate the finite-difference traveltime tables for P- and S-waves are discussed in Paulssen et al. (1992) and Reamer and Hinzen (2004). The hypocenter solutions and their uncertainties for a M1.2 event and the M5.8 earthquake are presented in Figs. 16 and 17, respectively. Plot B in Fig. 12 shows the recorded waveforms of the M1.2 event. The station distances are much longer compared to the previous case studies for the induced earthquakes leading to larger hypocenter uncertainties. Both events are found to have a hypocenter in the lower crust. The depth of the hypocenter of the M5.8 earthquake is estimated to be around 25 km. Paulssen et al. (1992) calculated the depth to be around 20–21 km based on an inversion with P-wave onsets only. The KNMI hypocenter is set to 15 km. The depths of the two tectonic events estimated in this work are both found to be 10 km deeper

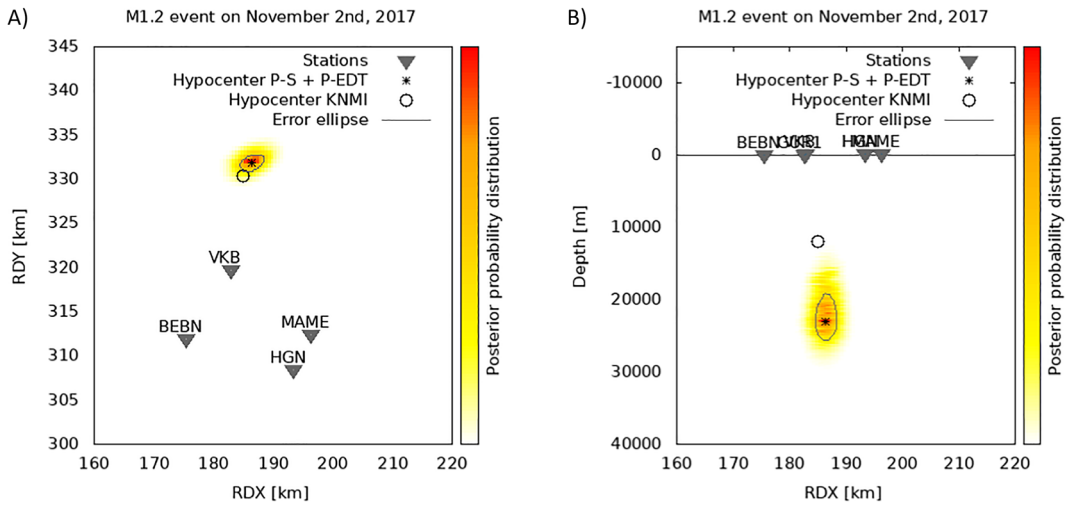

Fig. 16 Hypocenter analysis of tectonic earthquake. **A** and **B** are the horizontal and vertical cross-sections of the M1.2 event. The format and symbols are the same as in Fig. 7

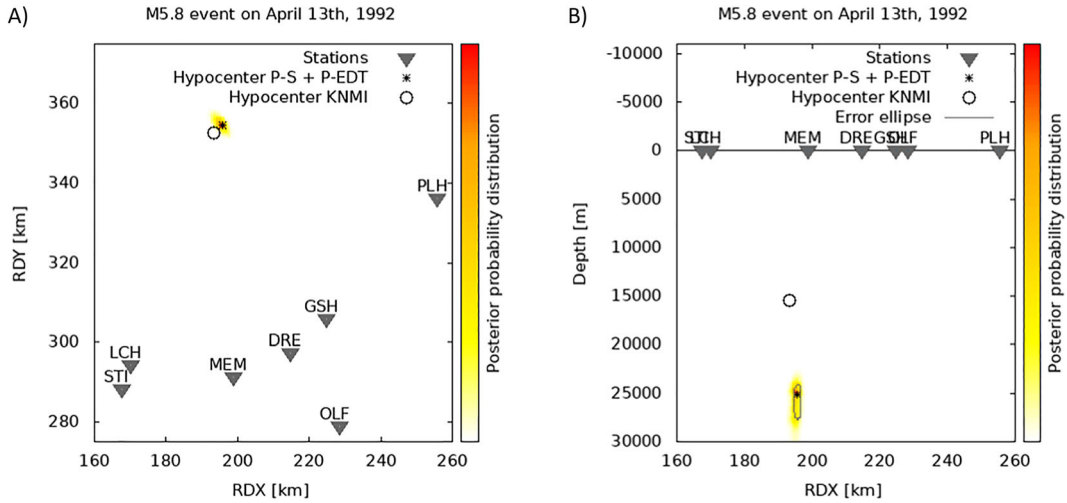

Fig. 17 Hypocenter analysis of tectonic earthquake. **A** and **B** are the horizontal and vertical cross-sections of the M5.8 event near Roermond, the Netherlands. The format and symbols are the same as in Fig. 7

than the official KNMI hypocenters. This discrepancy in depth can be explained by the difference in hypocenter methodology and velocity profile. The velocity profile for the area with tectonic earthquakes which is used here was derived in a tomographic experiment by Reamer and Hinzen (2004). The velocity profile for the south of the Netherlands in the KNMI seismological operations is an average model to fit the purpose of a larger region with different kinds of geological settings. In addition, it is noted that the depth sensitivity of the seismic wavefield decreases for stations farther away from the source which may have some effect on the hypocenter solution of the M5.8 event in Roermond.

An example of hypocenter relocation of three other detected events in Limburg is found in Spetzler (2023). The official KNMI hypocenter depth was fixed to 1 km, a solution attributed by the current setup and velocity profile in the daily operations. The Dutch regulator *The State Supervision of Mines* was concerned that the three events were caused by past mining activities in the area (Cuenca et al. 2013). The issue was solved by a new analysis of the events based on the improved hypocenter method and velocity profile for Limburg. The source depth of these earthquakes was found to be around 11 km. The three earthquakes were characterised as having a tectonic origin.

6 Discussion and conclusions

We have investigated how to improve the methodology for hypocenter analysis of earthquakes. The essential components in the earthquake location process are the engine to calculate traveltimes in the hypocenter method, the optimisation approach to find the hypocenter and the estimation of the uncertainty of the source location.

For the traveltime calculations, we compared the FMM method by Podvin and LeComte (1991) with FD simulations. Traveltimes were extracted from the FD waveforms by kurtosis. The FMM approach in the open-source Non-Lin-Loc software offers an effortless way to calculate traveltimes for P- and S-waves in relatively complex 3D media. However, there are limitations to the use of the FMM method for increasing complex structures. We validated the FMM method for two velocity profiles taken from a geological setting for tectonic earthquakes and a region with induced seismicity. For the case of tectonic earthquakes where the model consists of increasing velocities for increasing depth and relative small velocity contrasts, it was sufficient to use the FMM to calculate P- and S-wave traveltime functions. However, for the demonstration with the velocity profile for induced events, the elas-

tic model has a strong velocity increment due to a thick salt formation sealing the top of the reservoir. The FMM failed for epicentral distances larger than 3–4 km. For that reason, the P- and S-wave traveltime tables were calculated with finite-difference waveform simulations to account for all wave phenomena.

The FMM method and FD with the kurtosis approach to calculate traveltime functions with an epicentral distance and depth dependence can be calculated on a modern desktop computer. The traveltimes are quickly calculated with pre-defined traveltime functions for P- and S-waves. The hypocenter analysis can be carried out with a common grid search method which as well allows to quickly calculate the posterior probability distribution. The spatially distributed objective function is required to estimate the uncertainty of the hypocenter location. The error ellipse for the hypocenter is defined as one standard deviation of the posterior probability distribution and is derived from the 95 % percentile volume.

To reduce the hypocenter uncertainty, the established hypocenter approach based on either P-S phase difference per station or P-phase difference between pairs of stations has been combined to use both phase difference attributes simultaneously. The result is that the uncertain in epicenter is reduced mainly with the effect of P-phase differences between two stations while the smallest error in the depth is coming from the P-S traveltime differences. The hypocenter uncertainty accounts for errors in the background velocity model, modelling, instrumentation and phase picking.

The hypocenter method was tested on different seismological events types and geological settings. For the case studies of induced earthquakes, production with either injection or extraction of fluids can locally change the stress regime. For example for induced earthquakes in the Groningen gas field, the extraction of gas has reduced the supporting pressure in the reservoir at 3 km depth. The massive overburden is pushing down on pre-existing faults in the reservoir which at some point exerts the critical failure point and an induced earthquake can take place (Wentinck and Kortekaas 2023). The induced earthquakes in the gas storage facility in salt diapirs are again likely caused by the overburden adding pressure on the upper part of the dome with caverns inside (Bosq 2020). The site near Venlo is characterised by faults in the subsurface which initially was favourable for the fluid flow in the doublet system. Unfortunately, the nearby faults were re-activated by injecting water into the subsurface (Vörös and Baisch 2022). The region between the Netherlands, Germany and Belgium has a mixture of a complex horst and graben structure and past mining activities. For this region, the important question is whether events are of an induced or tectonic origin. In a preliminary study of the set of detected events in Limburg using the hypocenter approach presented in this work, we found that indeed many events in the Ruhr Valley Graben area are located in the middle-to-lower crust. The large depth (>20 km) of some of the events points to a considerable depth of the brittle-to-ductile transition. For other areas further south towards the borders between the Netherlands, Germany and Belgium, we have found that detected events tend to have depths in the upper-to-mid crust. The study of the seismicity in the border region between the Netherlands, Germany and Belgium is too extensive to describe in details in this paper. Hinzen et al. (2021) provide an overview of recent seismicity in this area.

With a well-defined hypocenter and error ellipse, it is likely possible to differentiate whether a detected event would be induced or tectonic based on the depth estimate. Equally, accurate hypocenters of tectonic events can help to distinguish between different geological settings or stress field regimes. The examples of real induced and tectonic events in this work show that the P-S and P-EDT method is capable of accurate hypocenter determination with valuable information about location uncertainty.

Acknowledgements The involvement of Hugues Dijkpesse in the development of the hypocenter uncertainty methodology is acknowledged by the authors. ER worked in an intern project supervised by Hugues. JS met Hugues when both were students in the group of Albert Tarantola in 1995 in Paris. DB implemented the kurtosis methodology by Baillard et al. (2014) during an internship at the KNMI. She extracted P- and S-phase arrivals from waveforms of induced earthquakes in Groningen. The kurtosis program is used in this study to estimate the first arrivals of P- and S-waves from the finite-difference waveform simulations to construct traveltime tables. Pauline Kruiver from the Royal Netherlands Meteorological Institute proof read the manuscript. The editor Klaus Hinzen and the two reviewers, Joachim Ritter and one anonymous, are acknowledged for their good suggestions that helped to improve the paper.

Author contributions Not applicable.

Availability of data and materials Netherlands Seismic and Acoustic Network. Royal Netherlands Meteorological Institute (KNMI). A description of the hypocenter method and velocity profiles in the seismological operations is made available.

Code availability A Python program is provided to perform the hypocenter analysis for a constant velocity model.

Declarations

Conflict of interest The authors declare no competing interests.

Ethics approval Not applicable.

Consent to participate Not applicable.

Consent for publication Not applicable.

References

Aki K, Richards PG (1980) Quantitative seismology, theory and methods. Freeman and Company

Baillard C, Crawford WC, Ballu V, Hibert C, Mangeney A (2014) An automatic kurtosis-based P-and S-phase picker designed for local seismic networks. Bull seism Soc Am 104:1–16. https://doi.org/10.1785/0120120347

Bardainne T, Dubos-Sallee N, Senechal G, Mangeney A (2008) Analysis of the induced seismicity of the Lacq gas field (Southwestern France) and model of deformation. Geophys J Int 173:1151–1162. https://doi.org/10.1111/j.1365-246X.2007.03705.x

Bosq H (2020) Using continuous microseismic surveillance for the management of cavern fields. SMRI Fall 2020 Virtual Technical Conference

Camelbeeck T, Vanneste K, Verbeeck K, Moreno D, Van Noten K, Lecocq T (2020) How well does known seismicity between the lower Rhine Graben and southern North Sea reflect future earthquake activity? Historical Earthquakes, Paleoseismology, Neotectonics and Seismic Hazard: New Insights and Suggested Procedures 18:52–74. https://doi.org/10.23689/fidgeo-3866

Cuenca MC, Hooper AJ, Hanssen RF (2013) Surface deformation induced by water influx in the abandoned coal mines in Limburg, The Netherlands observed by satellite radar interferometry. J Appl Geophys 88:1–11. https://doi.org/10.1016/j.jappgeo.2012.10.003

Dahm T, Cesca S, Hainzl S, Braun T, Krüger F (2015) Discrimination between induced, triggered, and natural earthquakes close to hydrocarbon reservoirs: a probabilistic approach based on the modeling of depletion-induced stress changes and seismological source parameters. J Geophys Res Solid Earth 120:2491–2509. https://doi.org/10.1002/2014JB011778

Dando BDE, Oye V, Näsholm SP, Zühlsdorff L, Kühn D, Wuestefeld A (2019) Complexity in microseismic phase identification: full waveform modelling, traveltime computations and implications for event locations within the Groningen gas field. Geophys J Int 217:620–649. https://doi.org/10.1093/gji/ggz017

de Jager J, Visser C (2017) Geology of the Groningen field-an overview. Neth J Geosci 96(5):3–15. https://doi.org/10.1017/njg.2017.22

Dost B, Ruigrok E, Spetzler J (2017) Development of seismicity and probabilistic hazard assessment for the Groningen gas field. Neth J Geosci 96(5):235–245. https://doi.org/10.1017/njg.2017.20

Eaton D, Eyre TS (2018) Induced seismicity in Western Canada: causes and consequences. Conference: Geohazards

Font Y, Kao H, Lallemand S, Liu CS, Chiao LY (2004) Hypocentral determination offshore eastern Taiwan using the maximum intersection method. Geophys J Int 158:655–675. https://doi.org/10.1111/j.1365-246X.2004.02317.x

Geiger L (1912) Probability method for the determination of earthquake epicenters from the arrival time only. Bull St Louis Univ 8:60–71

Grigoli F, Cesca S, Rinaldi AP, Manconi A, Lopez-Comino JA, Clinton J, Westaway R, Cauzzi C, Dahm T, Wiemer S (2018) The November 2017 M_w 5.5 Pohang earthquake: a possible case of induced seismicity in South Korea. Science 360:1003–1006. https://doi.org/10.1126/science.aat2010

Hinzen KG, Reamer SK, Fleischer C (2021) Seismicity in the Northern Rhine Area (1995–2018). J of Seis 25:351–367. https://doi.org/10.1007/s10950-020-09976-7

Jocker J, Spetzler J, Smeulders D, Trampert J (2006) Validation of first-order diffraction theory for the traveltimes and amplitudes of propagating waves. Geophysics 71:167–177. https://doi.org/10.1190/1.2358412

Lienert BR, Berg E, Frazer LN (1986) Hypocenter: an earthquake location method using centered, scaled, and adaptively damped least squares. Bull seism Soc Am 76(3):771–783. https://doi.org/10.1785/BSSA0760030771

Lomax A (2005) A reanalysis of the hypocentral location and related observations for the great 1906 California earthquake. Bull seism Soc Am 95:861–877. https://doi.org/10.1785/0120040141

Netherlands seismic and acoustic network. Royal Netherlands Meteorological Institute (KNMI). Other/Seismic Network. https://doi.org/10.21944/e970fd34-23b9-3411-b366-e4f72877d2c5

OpenStreetMap contributors (2017) Planet dump retrieved from https://planet.osm.org

Paulssen H, Dost B, van Echt T (1992) The April 13, 1992 earthquake of Roermond (The Netherlands); first interpretation of the NARS seismograms. Geol Mijnbouw 71:91–98

Podvin P, Lecomte I (1991) Finite difference computation of traveltime in very contrasted velocity models: a massively parallel approach and its associated tools. Geophys J Int 105:271–284. https://doi.org/10.1111/j.1365-246X.1991.tb03461.x

Pyle ML, Chen T, Presten L, Scalise M, Zeiler C, Smith KD (2023) How good Is your location? Comparing and understanding the uncertainties in location for the 1993 Rock Valley sequence. The Seismic Record 3(4):259–268. https://doi.org/10.1785/0320230025

Reamer SK, Hinzen KG (2004) An earthquake catalog for the northern Rhine Area, Central Europe (1975–2002). Seismol Res Lett 75:713–725. https://doi.org/10.1785/gssrl.75.6.713

Reshetnikov A, Kummerow J, Asanuma H, Haring M, Shapiro SA (2015) Microseismic reflection imaging and its application to the Basel geothermal reservoir. Geophysics 80:39–49. https://doi.org/10.1190/GEO2014-0593.1

Robertsson JOA, Blanch JO, Symes WW (1994) Viscoelastic finite-difference modeling. Geophysics 59:1444–1456. https://doi.org/10.1190/1.1443701

Romijn R (2017) Groningen velocity model 2017-Groningen full elastic velocity model September 2017. Technical Report, www.namplatform.nl

Ruigrok E, Kruiver P, Dost B (2023) Construction of earthquake location uncertainty maps for the Netherlands. KNMI Technical report 405. https://cdn.knmi.nl/knmi/pdf/bibliotheek/knmipubTR/TR405.pdf

Satriano C, Lomax A, Zollo A (2008) Real-time evolutionary earthquake location for seismic early warning. Bull seism Soc Am 98:1482–1494. https://doi.org/10.1785/0120060159

Savvaidis A, Lomax A, Breton C (2020) Induced seismicity in the Delaware basin, West Texas, is caused by hydraulic fracturing and wastewater disposal. Bull seism Soc Am 110:2225–2241. https://doi.org/10.1785/0120200087

Schmittbuhl J, Lambotte S, Lengline O, Grunberg M, Jung H, Vergne J, Cornet F, Doubre C, Masson F (2021) Induced and triggered seismicity below the city of Strasbourg, France from November 2019 to January 2021. Compte Rendus Geoscience 353:561–584

Schoenball M, Ellsworth WL (2017) A systematic assessment of the spatiotemporal evolution of fault activation through induced seismicity in Oklahoma and Southern Kansas. J Geophys Res, Solid Earth 122:10189–10206. https://doi.org/10.1002/2017JB014850

Smith JD, White RS, Avouac JP, Bourne S (2020) Probabilistic earthquake locations of induced seismicity in the Groningen region, The Netherlands. Geophys J Int 222:507–516. https://doi.org/10.1785/0120060159

Soler T, Chin M (1985) On transformation of covariance matrices between local Cartesian coordinate systems and commutative diagrams. 45th Annual Meeting ASP-ACSM Convention Washington, DC: American Congress on Surveying & Mapping 393–406

Spetzler J (2023) Hypocenters for the events between March and May 2023 near Klimmen. KNMI Technical report 404. https://cdn.knmi.nl/knmi/pdf/bibliotheek/knmipubTR/TR404.pdf

Spetzler J, Dost B (2017) Hypocenter estimation of induced earthquakes in Groningen. Geophys J Int 209:453–465. https://doi.org/10.1093/gji/ggx020

Spetzler J, Snieder R (2004) The Fresnel volume and transmitted waves. Geophysics 69:653–663. https://doi.org/10.1190/1.1759451

Spetzler J, Sivaji C, Nishizawa O, Fukushima Y (2002) A test of ray theory and scattering theory based on a laboratory experiment using ultrasonic waves and numerical simulation by finite-difference method. Geophys J Int 148:165–178. https://doi.org/10.1046/j.1365-246X.2002.01552.x

Spetzler J, Ruigrok E, Dost B, Evers L (2018) Hypocenter Estimation of Detected Event near Venlo on September 3rd 2018. KNMI Technical report 369. https://cdn.knmi.nl/knmi/pdf/bibliotheek/knmipubTR/TR369.pdf

Spetzler J, Snieder R (2001) The effect of small scale heterogeneity on the arrival time of waves. Geophys J Int 145:786–796. https://doi.org/10.1046/j.1365-246x.2001.01438.x

Strutt JW, Rayleigh B (1926) The theory of sound (reprinted by Mac-Millan, London (1926), 1877) 1:150–157

Tarantola A (1987) Inverse problem theory: methods for data fitting and model parameter estimation. Elsevier

Theunissen T, Font Y, Lallemand S, Gautier S (2012) Improvements of the maximum intersection method for 3D absolute earthquake locations. Bull Seism Soc Am 102:1764–1785. https://doi.org/10.1785/0120100311

van Dalfsen W, Doornenbal JC, Dortland S, Gunnink JL (2006) A comprehensive seismic velocity model for the Netherlands based on lithostratigraphic layers. Neth J Geosci 85(4):277–292. https://doi.org/10.1017/S0016774600023076

Vanneste K, Camelbeeck T, Verbeeck K (2012) A model of composite seismic sources for the lower Rhine Graben, northwest Europe. Bull. Seism Soc Am 103:984–1007. https://doi.org/10.1785/0120120037

Vörös R, Baisch S (2022) Induced seismicity and seismic risk management-a showcase from the Californië geothermal field (the Netherlands). Neth J Geosci 101:e15. https://doi.org/10.1017/njg.2022.12

Waldhauser F, Ellsworth WL (2000) A double-difference earthquake location algorithm: method and application to the Northern Fault, California. Bull Seism Soc Am 90:1353–1368. https://doi.org/10.1785/0120000006

Wang B, Shi W, Miao Z (2015) Confidence analysis of standard deviational ellipse and its extension into higher dimensional Euclidean space. PLoS ONE 10(3):1–17. https://doi.org/10.1371/journal.pone.0118537

Wentinck HM, Kortekaas M (2023) Induced seismicity in the Groningen gas field-arrest of ruptures by fault plane irregularities. Neth J Geosci 102:e11. https://doi.org/10.1017/njg.2023.9

Willacy C, van Dedem E, Minini S, Li J, Blokland JW, Das I, Droujinine A (2019) Full-waveform event location and moment-tensor inversion for induced seismicity. Geophysics 84:39–57. https://doi.org/10.1190/geo2018-0212.1

Willacy C, Blokland JW, van Dedem E (2020) Automatic event location monitoring for induced seismicity. Lead Edge 39:505–512. https://doi.org/10.1190/tle39070505.1

Zaliapin I, Ben-Zion Y (2016) Discriminating characteristics of tectonic and human-induced seismicity. Bull Seism Soc Am 106:846–859. https://doi.org/10.1785/01200150211

Zhang H, Thurber C (2006) Development and application of double-difference seismic tomography. Pure Appl Geophys 163:373–403. https://doi.org/10.1007/s00024-005-0021-y